The International Journal of Advanced Manufacturing Technology (2022) 119:5079–5093
https://doi.org/10.1007/s00170-021-08556-4

ORIGINAL ARTICLE

Experimental and analytical study on adiabatic shear localized fracture characteristics in high-speed machining of pure titanium alloy

Liyao Gu[1] · **Minjie Wang**[2]

Received: 13 August 2021 / Accepted: 11 December 2021 / Published online: 14 January 2022

Abstract

The characteristics of adiabatic shear localized fracture in high-speed machining of pure titanium alloy were further investigated experimentally and analytically. The formation laws of isolated segment chip were revealed under high cutting speeds, negative rake angles, and large feeds. The damage process of adiabatic shear localized fracture was analyzed through microscopic observations on the fractured surface of isolated segment. Considering the pre-peak and post-peak constitutive relations, a thermo-visco-plastic constitutive model with kinematics hardening algorithm was developed into finite element subroutine. Considering the energy dissipation in the propagation of adiabatic shear band, the energy criterion of adiabatic shear localized fracture was further applied in the constitutive model. The simulated formation process of isolated segment chip and the corresponding cutting forces were verified and discussed. The results showed that the austenite grains in shear band material were tore to small pieces and the austenite twins were observed in the chip segment. The cold welding effect between the fractured segment surfaces suppressed the free surface cracking. High cutting speed induced strengthening effect leads to abrupt brittle-ductile fracture in adiabatic shear band. Higher fluctuation amplitude of cutting force and lower average cutting force were found in isolated segment chip formation.

Keywords High-speed machining · Adiabatic shear localized fracture · Isolated segment chip · Kinematics hardening algorithm · Finite element analysis

1 Introduction

High-speed machining (HSM) is an efficient material removing technology with the advantages of high efficiency and good surface quality in most manufacturing fields. Under high cutting speed, the work material is inevitably subjected to the large and fast heating and deforming. Under such extreme loading environment, adiabatic shear evolution from instability to fracture tends to occur, transforming serrated chips to isolated segment chips. As the final stage of adiabatic shear evolution, the occurrence of adiabatic shear localized fracture (ALSF) in adiabatic shear bands (ASBs) inevitably influences the performances of machinability, such as chip morphology, cutting force, and energy dissipation. Although the fracture mechanism of serrated chip was studied in most existing experimental works, the ALSF mechanisms of titanium alloy under high cutting speed are rarely involved. Therefore, the transient fracture mechanisms and the critical characteristics of ALSF in isolated segment chip formation need further investigations through appropriate analytical models.

A few studies developed some constitutive models in finite element analysis on machining of titanium alloys. Three modified Johnson–Cook models (JCM) without damage condition were built by Sima and Özel [1] to simulate the process of adiabatic shearing in serrated chip of Ti6Al4V with the carbide cutting tools. Based on JCM and its damage criterion in the subsequent studies, Zhang et al. [2] built a finite element model with thermo-mechanical coupling condition to explore the chip morphology transition under different cutting parameters. Wu and To [3] found the sensitivity of tool angle to the serrated chip formation in machining of TC21 titanium alloy. Modifying the components of strain hardening and strain rate strength of JCM by using the Fortran routine

✉ Liyao Gu
guliyao0922@163.com

[1] School of Mechanical Engineering & State Key Laboratory of Traction Power, Southwest Jiaotong University, Chengdu, China

[2] School of Mechanical Engineering, Dalian University of Technology, Dalian, China

via available interface, Hokka et al. [4] compiled the isotropic hardening model, He et al. [5] simulated the flow stress of serrated chip in machining of Ti6Al4V, and Gao et al. [6] developed a stress-updating algorithm to construct a HCP model via Abaqus/Explicit software. Shuang et al. [7] improved the simulated model with both the hyperbolic tangent law and the Johnson–Cook law in machining of Ti6Al4V. Calamaz et al. [8] built a hyperbolic tangent model (HTM), and Che et al. [9] considered the material defects via JC-THAN model.

Some failure criterions were developed in analyzing the fracture mechanisms of serrated chip. Guo and Yen [10] applied the JCM and its damage model, and Hua and Shivpuri [11] applied JC damage model to simulate the process of crack propagation and the stress field in serrated chip. The chip flowing behavior of titanium alloy was simulated by Ye et al. [12], and the balance conditions between the kinetic and surface energies were analyzed by Ma et al. [13]. Wang and Liu [14] adopted the JCM with Hillerborg fracture energy criterion in simulating the machining process of Ti6Al4V. Cui et al. [15] investigated the discontinuous chips of hardened steel through the JC damage model and Atlati contact model.

In the present work, through the high-speed machining experiments and the quick-stop tests of α-pure titanium alloy, the cutting conditions of isolated segment chip formation under the various cutting speeds, negative rake angles, and large feeds are obtained, and the damage characteristics of ASLF are analyzed microscopically. The thermo-visco-plastic constitutive model with the pre-peak and post-peak constitutive relations is developed into finite element subroutine. The saturation limit energy criterion of ASLF is further deduced and applied in the finite element analysis. The isolated segment chip formation in the fracture process is simulated, and the corresponding cutting forces are verified and discussed.

2 Experiment processes

TA2 alloy, a typical α-pure titanium alloy, is an important biomaterial for the excellent biocompatible performance and was selected as the workpiece material. Its physical parameters are of high specific strength and low thermo-physical property as shown in Table 1. The heat treatment processes, vacuum annealing (520 ℃) and temperature holding (9 min), were made to relax the residual stress and improve the machining performance. The obtained metallographic structure was austenite block (Fig. 1) with the hardness of 58 HRA.

The triangular PCBN inserts were used under dry condition with OKUMA mill-turn machine tool. The cylindrical workpiece with diameter of 200 mm and thickness of 2 mm

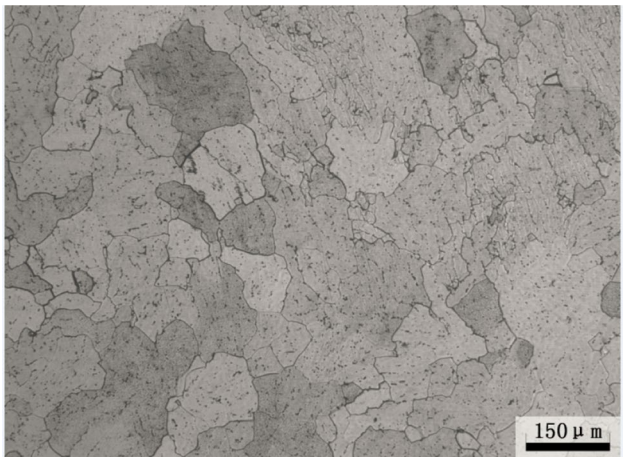

Fig. 1 Metallographic structure of α-pure titanium alloy

was made to meet the plane-strain condition in orthogonal machining tests. The uncut thickness was accurately controlled by the feed rate and the tool edge detector. The cutting speed was ~ 1600 m/min, the feed rate was 0.2 mm/r, and the tool rake angle was −10° ~ −20°. The chip specimens obtained from the experiments were cleaned ultrasonically and observed by metallographic microscope, and the fractured surfaces of isolated segment were observed by scanning electron microscope (SEM).

In order to analyze the ASB fracture process between the chip segments, the quick-stop device [16] are shown in Fig. 2a. The quick-stop workpieces (QSWs) were fixed with the workpiece fixture which was held with the lath chuck. When the rotating spindle attained to the required speed, the insert fed forward to the predefined position to arrest the chip root. As illustrated in the quick-stop principle (Fig. 2b), the cutting speed is v, the feed is f, and the times t_0 and t_f are the initial and finish times of obtaining chip root, respectively. Due to the machined hole in the QSW, the cutting stress σ_{cut} attains to the tensile strength σ_b at the time t_f. The arresting acceleration can be attained to $10^6 \sim 10^7$ m/s^2 under the cutting speed nearly 10^3 m/min due to the small mass of chip root. The chip roots were cleaned ultrasonically and observed by metallographic microscope.

3 Experiment results

3.1 Chip morphology

The typical chip morphology development of α-pure titanium alloy under negative rake angle of −10° with the

Table 1 Physical and mechanical parameters of α-pure titanium alloy

ρ(kg/m^3)	c(J/kg·K)	k(W/m·K)	E(GPa)	v	σ_b(MPa)	σ_s(MPa)	δ(%)	φ(%)
4510	480	19.3	107.9	0.34	500	435	29	43

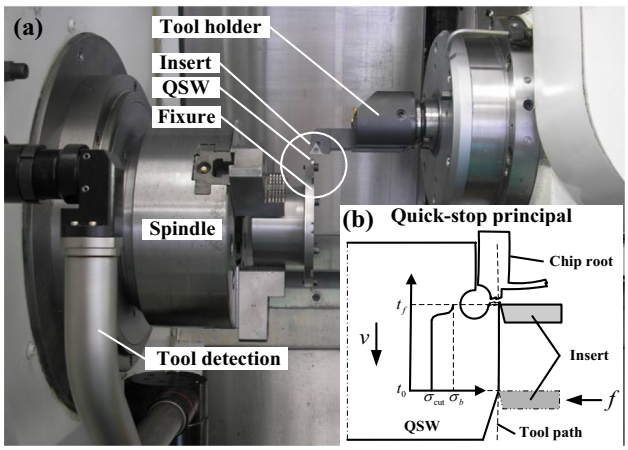

Fig. 2 Quick-stop device and its quick-stop principle

increase of cutting speed is shown in Fig. 3. The material in generated chip experienced the process of adiabatic shear evolution that includes general shear flow in ribbon chip (Fig. 3a), adiabatic shear flow in deformed bands (DBs) and transformed bands (TBs) in serrated chip from the cutting speeds of 60 ~ 200 m/min (Fig. 3a–c), cracks formation and propagation in TBs (Fig. 3d and e), and complete fracture along TBs forming isolated segment chips when the cutting speeds attained 1600 m/min (Fig. 3f). The influence of cutting speed and feed on chip morphology under negative rake angles of − 10° and − 20° is shown in Fig. 4. We found that ASLF-induced isolated segment chip formation was prone to occur under negative rake angle and large feed which shortened the speed range of adiabatic shear evolution. Gu et al. [17] found that negative rake angle increased the pressure and friction imposed on chip surface. Accordingly, α-pure titanium alloy is an ASLF sensitive material to pressure stress under negative rake angle. Gente et al. [18] found that the ASLF of titanium alloy were not sensitive under the small uncut thickness. The small uncut thickness easily leaded to distinct softening effect in the chip material, resulting in the reinforcement of fracture toughness of shear band under high cutting temperature.

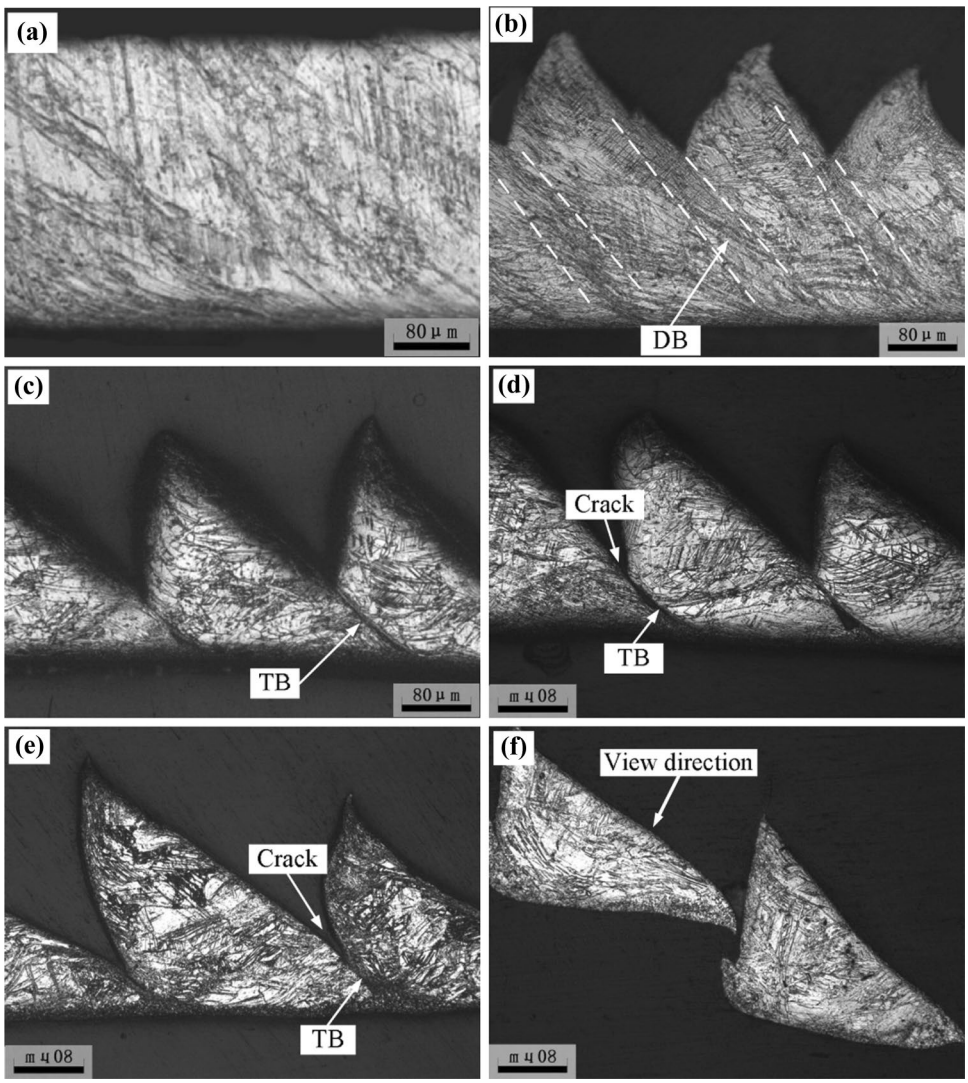

Fig. 3 Typical chip morphology development companying with adiabatic shear evolution in high-speed machining of α-pure titanium alloy. (**a**) Ribbon chip at 30 m/min; (**b**) serrated chip with DBs at 60 m/min; (**c**) serrated chip with TBs at 200 m/min; (**d**) serrated chip with cracks in TBs at 500 m/min; (**e**) serrated chip with cracks in TBs at 800 m/min; (**f**) isolated segment chip at 1600 m/min

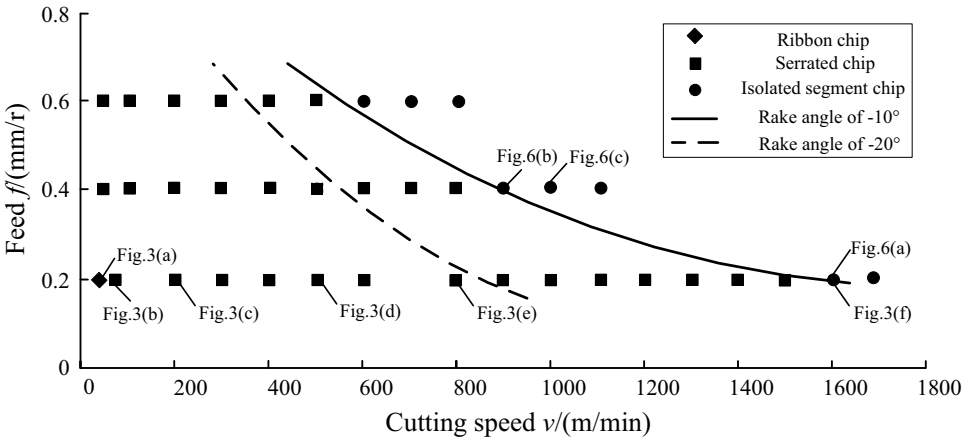

Fig. 4 Experimental results of chip morphology with the cutting speed and feed under negative rake angles in high-speed machining of α-pure titanium alloy

The TBs formation in Fig. 3c and its sharp-tip crack propagation in ASB in Fig. 3d under larger magnification are shown in Fig. 5. The intense plastic flowing in transformed band occurs as shown in Fig. 5a. The austenite grains in shear band were tore to small pieces, and the austenite twins could be observed in the chip segment. Due to the poor heat dissipation, thin shear bands were formed under higher cutting speed, resulting in an increase of adiabatic shear sensitivity. Subsequently, the ductility of ASB decreases so that sharp-tip cracks formed and brittle fracture took place in ASB, as shown in Fig. 5b. Although the trace of sliding line due to plastic flowing was found near the boundary of shear band, the fragmentation of austenite grains in the shear band was more serious due to the weakening effects, including thermal softening, phase transition, and degenerating.

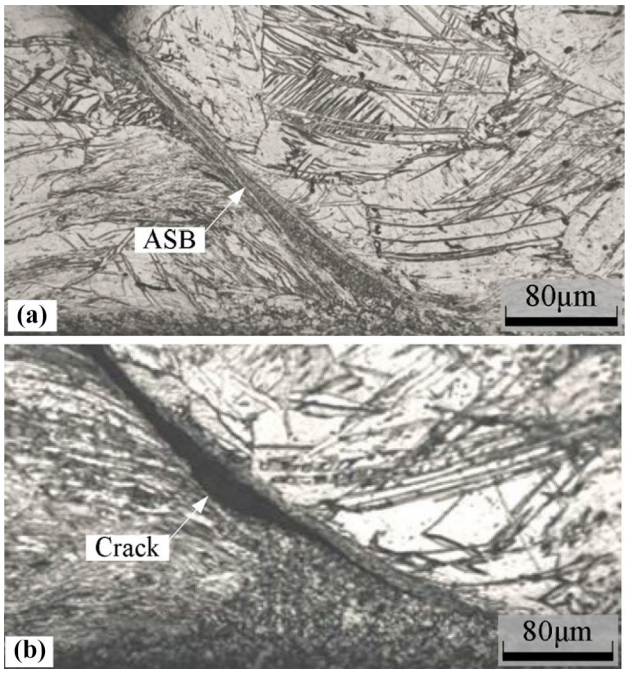

Fig. 5 (**a**) TBs formation and (**b**) its sharp-tip crack propagation in ASB during high-speed machining of α-pure titanium alloy

3.2 Damage and fracture in ASB

The damage and fracture mechanisms in ASB were inspected through observing the single fractured segment surface via SEM. The observation results are illustrated in Fig. 6. According to the view direction in Fig. 3f, the dimple region, smooth region, and the transition region are examined as shown in Fig. 6a. The dimple structure on the fractured surface is usually considered as the mark of ductile fracture which was also observed on the fracture surface of serrated chip [19] and cup-cone sample in impact test [20]. Due to the FCC crystal structure of titanium gains and the temperature and stress states near the tool tip, the dimple structure was gradually faded away, forming smooth surface. The transition region from dimple surface to smooth surface was relatively lager at small feed due to the remarkable thermal softening effect (Fig. 6a, c). It was indicated that the thermal softening effect was more obvious under smaller feed due to the occurrence of ASLF. The melting state has not been found on the fractured ASB surface in the SEM observation. The dimple structure means the ductile fracture via voids nucleation and coalescence, and the smooth region means the brittle fracture via sharp-tip crack propagation. Thus, the ductile–brittle transition is the ASLF damage characteristic of α-pure titanium alloy. In the first stage, the ductile voids nucleated from the inclusions, secondary phases, or defects in material. The growing voids were elongated under the pressure stress near the chip surface. In second stage, the coalescence of elongated voids leaded to ductile crack, generating transition surfaces with parabolic dimples. Finally, the smooth surface without melting trace was formed on the fractured surface due to the friction induced cold welding and subsequent cracking between the segments.

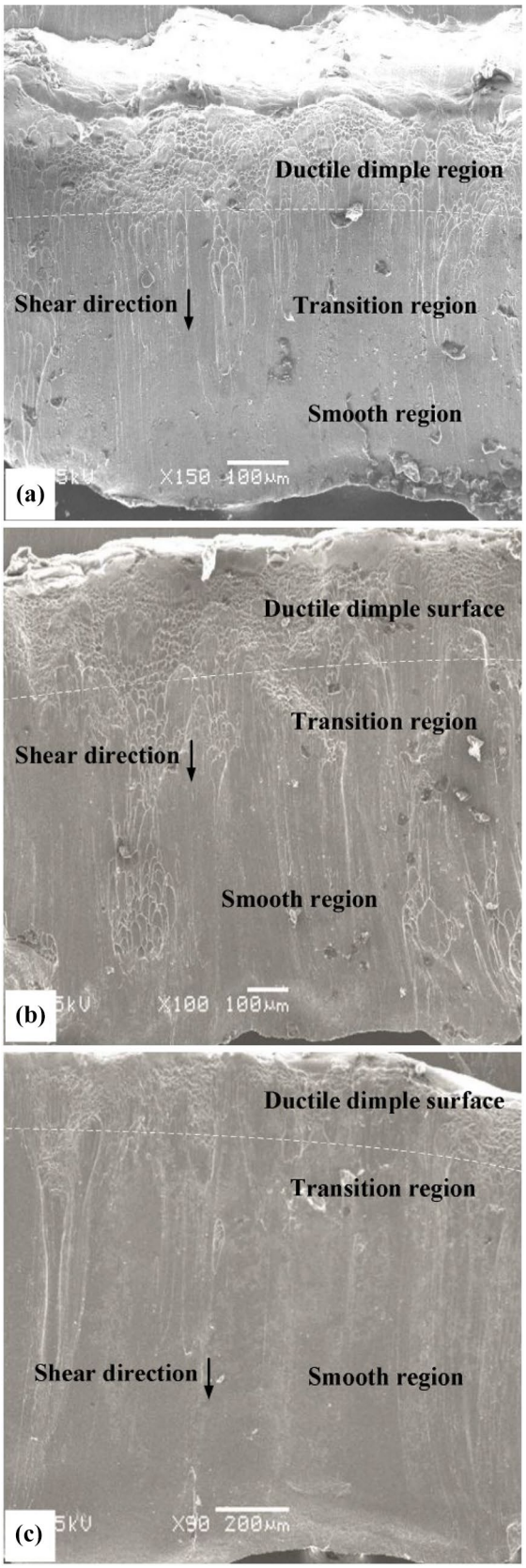

Fig. 6 Fracture surface observation results of isolated segment chip of α-pure titanium alloy: the distribution states of ductile dimple region, smooth region and the transition region

The multi-stage ASLF process in the chip root of α-pure titanium alloy was observed in Fig. 7. In first stage (Fig. 7a), the cutting tool pushed a segment upward along the tool rake surface, and the TBs between the segment and the workpiece material were formed. In second stage (Fig. 7b), with the tool cutting forward, the crack in the TBs formed and propagated from the upside of segment. Being different from other carbon steel and stainless steel, the color of TBs was dark comparing with the matrix. In final stage (Fig. 4c), the chip segment was completely fractured and separated from the workpiece, and the crystal structure in primary shear zone was still kept due to the localized fracture in ASB. The chip root observation results were similar as Gente et al. [18] who suggested that ASB was the fracture path of isolated segments. As for the brittle fracture in ASB, Elbestawi et al. [21] thought that the work hardening easily leaded to brittle cracks on free surface; Poulachon and Moisan [22] hold that the quenching brittle effect resulted from the heat treatment. It was inferred that the complexity problem of ASLF mechanism was still unsolved through online detection method. Even so, these chip-root observation results provided an effective method for the post-investigation on the ASLF characteristics of α-pure titanium alloy.

4 Theoretical model

4.1 Constitutive framework

The evolution of ASB leads to the development of chip morphology from serrated chip to isolated segment chip in which complete fracture takes place along ASB. Considering the propagating effect of ASB in the fracture process, the high-speed machining model of isolated segment chip formation is illustrated in Fig. 8 which includes the models of serrated segment deformation [23], the distributions of velocity and strain rate in ASB, and the normal and shear stresses state. The meanings of the parameters in the figures are provided in the Appendix.

From the continuum point of view in the finite element constitutive framework, the total deformation of chip material is decomposed into elastic part and plastic part. The negligible elasticity part is taken into account in the whole deformation process. Accordingly, there exists a direct manner to define the plastic deformation. The constitutive governing equations from elasticity to plasticity are classically given as follows:

$$\begin{cases} \boldsymbol{\varepsilon}^p = \boldsymbol{\varepsilon} - \boldsymbol{\varepsilon}^e \\ \boldsymbol{\varepsilon}^e = \mathrm{D}^{-1} : \boldsymbol{\sigma}^e \\ \triangle\, \boldsymbol{\varepsilon}^p = \triangle\, \lambda \mathrm{n} \\ f_s = \frac{1}{2}(\mathrm{s} - \boldsymbol{\alpha}) : (\mathrm{s} - \boldsymbol{\alpha}) - \frac{1}{3}\sigma_s^2 \geq 0 \end{cases} \tag{1}$$

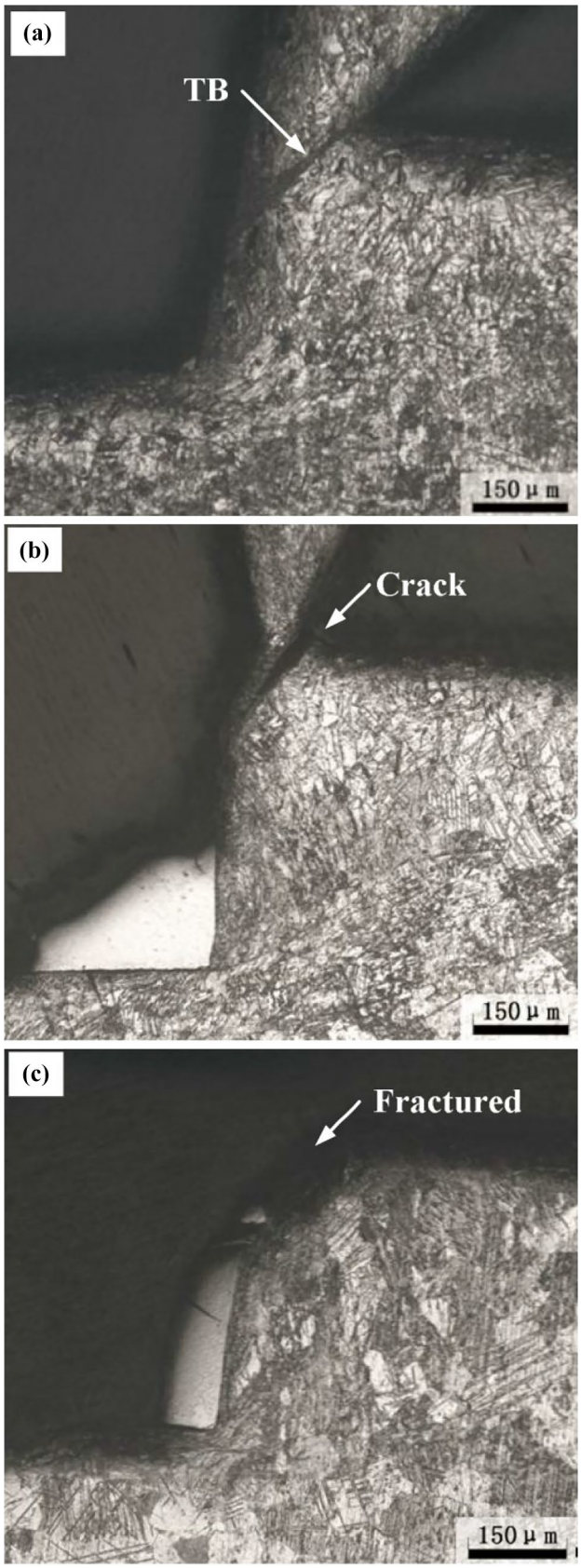

Fig. 7 The chip root observation results of the fracture process of isolated segment chip of α-pure titanium alloy at speed of 900 m/min and feed of 0.4 mm/r: (**a**) TB formation; (**b**) crack formation in ASB; (**c**) completely fracture in ASB

where $\boldsymbol{\sigma}, \boldsymbol{\varepsilon}, \dot{\boldsymbol{\varepsilon}}$ are stress tensor, strain tensor, and strain rate tensor, respectively. $\mathbf{D}$ is Hooke tensor. $\triangle$ represents time increment interval. $\triangle\ \lambda$ is plasticity scalar multiplier which can be determined through the yield condition. $f_s \geq 0$ is yield condition. $\mathbf{s}$ is deviator stress tensor. $\boldsymbol{\alpha}$ is cumulative plasticity resistance induced by plastic deformation. σ_s is plastic flow stress.

The plastic stage of chip material under the triaxiality stress state is considered according to von Mises yielding condition. We defined deviator stress tensor s, strain tensor $\boldsymbol{\varepsilon}$, and strain rate tensor $\dot{\boldsymbol{\varepsilon}}$ in the form of plastic flow stress σ_s, effective normal strain $\bar{\varepsilon}$, and effective normal strain rate $\dot{\bar{\varepsilon}}$ as:

$$\begin{cases} \mathbf{s} = \boldsymbol{\alpha} + \sqrt{\frac{2}{3}}\sigma_s \mathbf{n} \\ \boldsymbol{\varepsilon} = \sqrt{\frac{3}{2}}\bar{\varepsilon}\mathbf{n} \\ \dot{\boldsymbol{\varepsilon}} = \sqrt{\frac{3}{2}}\dot{\bar{\varepsilon}}\mathbf{n} \end{cases} \tag{2}$$

where $\mathbf{n} = (\mathbf{s} - \boldsymbol{\alpha})/\|\mathbf{s} - \boldsymbol{\alpha}\|$ is the unit yield vector. The effective normal stress $\bar{\sigma}$, the effective normal strain $\bar{\varepsilon}$, and the effective normal strain rate $\dot{\bar{\varepsilon}}$ are given in the form of principal stress components $[\sigma_i]$, principal strain components $[\varepsilon_i]$, and principal strain rate components $[\dot{\varepsilon}_i]$ as:

$$\begin{cases} \bar{\sigma} = \frac{1}{\sqrt{2}}\sqrt{\sum_{i,j=1,2,3}\delta_{ij}(\sigma_i - \sigma_j)^2} \\ \bar{\varepsilon} = \frac{\sqrt{2}}{3}\sqrt{\sum_{i,j=1,2,3}\delta_{ij}(\varepsilon_i - \varepsilon_j)^2} \\ \dot{\bar{\varepsilon}} = \frac{\sqrt{2}}{3}\sqrt{\sum_{i,j=1,2,3}\delta_{ij}(\dot{\varepsilon}_i - \dot{\varepsilon}_j)^2} \end{cases} \tag{3}$$

where δ_{ij} is Kronecker delta function. The principal stresses $[\sigma_i]$, principal strain $[\varepsilon_i]$, and principal strain rate $[\dot{\varepsilon}_i]$ are given in the form of the stress components, strain components, and strain rate components as:

$$\begin{cases} [\sigma_i] = \left[\frac{\sigma_y}{2} + (2-i)\sqrt{\frac{\sigma_y^2}{4} + \tau_{xy}^2}\right] \\ [\varepsilon_i] = \left[(2-i)\sqrt{\varepsilon_y^2 + \frac{\gamma_{xy}^2}{4}}\right] \\ [\dot{\varepsilon}_i] = \left[(2-i)\sqrt{\dot{\varepsilon}_y^2 + \frac{\dot{\gamma}_{xy}^2}{4}}\right] \end{cases} \tag{4}$$

where $\sigma_y = \tau_{xy}\cot\phi$ is the relation of shear stress and normal stress in ASB. $\phi = \arctan\left[\cos\gamma_0/(\zeta - \sin\gamma_0)\right]$ is

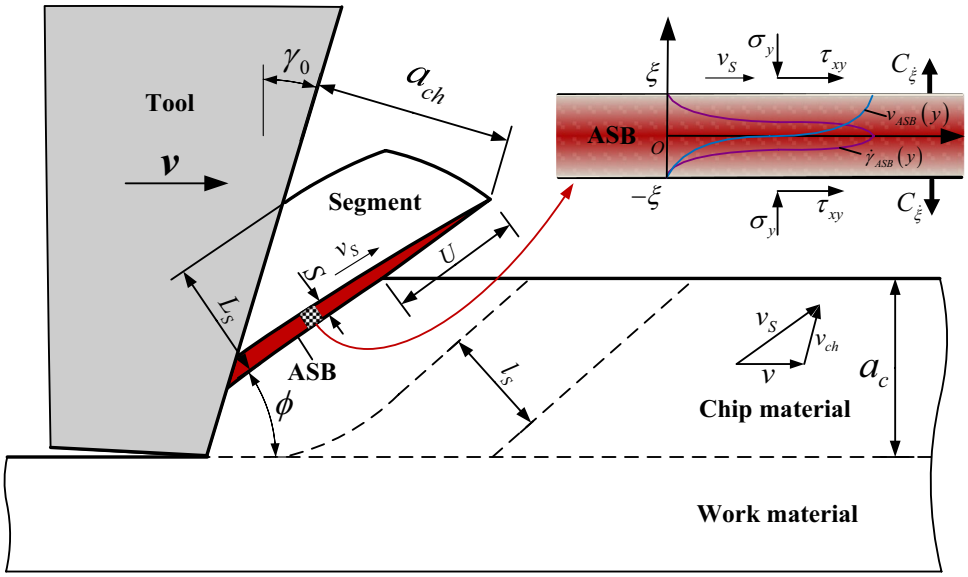

Fig. 8 High-speed machining model of isolated segment chip formation, including the models of serrated segment deformation, the distributions of velocity and strain rate in ASB, and the normal and shear stresses state

shear angle; $\zeta \approx 0.9 \sim 1.0$ is deformation coefficient of serrated chip.

The subscript of the tensor component is neglected in the following derivation. Considering von Mises yielding condition of shear deformation in ASB, the effective shear stress $\bar{\tau}$, effective shear strain $\bar{\gamma}$, and effective shear strain rate $\dot{\bar{\gamma}}$ can be expressed in the form of shear stress component τ, shear strain component γ, and shear strain rate component $\dot{\gamma}$ as:

$$\begin{cases} \bar{\tau} = \frac{\bar{\sigma}}{\sqrt{3}} = \frac{\tau}{2}\sqrt{\cot^2\phi + 4} \\ \bar{\gamma} = \sqrt{3}\bar{\varepsilon} = \gamma \\ \dot{\bar{\gamma}} = \sqrt{3}\dot{\bar{\varepsilon}} = \dot{\gamma} \end{cases} \tag{5}$$

In pre-peak plasticity stage, considering the relation of normal and shear stresses as well as the relation of normal and shear deformations, the effective shear stress $\bar{\tau}$ is the function of effective shear strain $\bar{\gamma}$, effective shear strain rate $\dot{\bar{\gamma}}$, and characteristic temperature θ^* in thermo-visco-plastic constitutive relation, generally expressed as:

$$\bar{\tau}\left(\bar{\gamma}, \dot{\bar{\gamma}}, \theta^*\right) = \frac{\sqrt{\cot^2\phi + 4}}{2\sqrt{3}} s_1\left(\frac{\gamma}{\sqrt{3}}\right) s_2\left(\frac{\dot{\gamma}}{\sqrt{3}}\right) s_3(\theta^*) \tag{6}$$

where $s_1 = A + B\left(\frac{\gamma}{\sqrt{3}}\right)^n$, $s_2 = 1 + C\ln\left(\frac{\dot{\gamma}}{\dot{\gamma}_0}\right)$, and $s_3 = m_1 \exp\left(m_2\theta^*\right)$ are the constitutive components of titanium alloy [24]. A, B, C, m_1, m_2 are constitutive parameters. $\theta^* = \left(\theta - \theta_0\right)/\left(\theta - \theta_M\right)$ is characteristic temperature. θ_0 and θ_M are initial and melting temperatures, respectively. The adiabatic temperature θ under high-speed machining is expressed as:

$$\theta = \frac{\beta\sqrt{\cot^2\phi + 4}}{2\rho c}\int_0^t \tau(\gamma, \dot{\gamma}, \theta^*)\dot{\gamma}dt + \theta_0 \tag{7}$$

where $\beta \approx 0.9$ is Taylor and Quinney coefficient.

In post-peak plasticity stage, according to the experimental analysis from Liao and Duffy [25] under high-speed impacting condition, the post-peak constitutive relation is linearized as:

$$\bar{\tau}\left(\bar{\tau}_p, \theta, D\right) = \bar{\tau}_p(1 - \alpha\theta)(1 - D) \tag{8}$$

where $\bar{\tau}_p = \max\left[\bar{\tau}\left(\bar{\gamma}, \dot{\bar{\gamma}}, \theta^*\right)\right]$ is peak shear stress, α is thermal weakening factor, $D = \bar{\tau}_p \Delta U / W_c$ is degenerating coefficient, U is shear band boundary displacement, and W_c is critical energy dissipation.

A kinematics hardening algorithm under high-speed machining condition is necessary to be developed into a finite element subroutine. A trail elastic stress in a strain increment $\Delta\boldsymbol{\varepsilon}$ is expressed as:

$$\mathbf{s}^*_{new} = \mathbf{s} + \lambda trace(\triangle\,\boldsymbol{\varepsilon})\mathbf{I} + 2\mu\,\triangle\,\boldsymbol{\varepsilon} \tag{9}$$

where λ and μ are Lamés constants. When the effective stress of trail elastic stress exceeds the yield stress, the strain increment $\Delta\boldsymbol{\varepsilon}$ as the plastic deformation $\triangle\,\boldsymbol{\varepsilon}^p$ occurs in the time increment. The stress increase or decrease due to plastic deformation in a time increment can be determined by the material hardening behavior. The linear plasticity hardening law $\triangle\,\boldsymbol{\alpha}$ applied in the following plastic increment is defined as:

$$\triangle\,\boldsymbol{\alpha} = \frac{2}{3}H\,\triangle\,\boldsymbol{\varepsilon}^p \tag{10}$$

where H is hardening effect which is the slope of plastic stress with strain, expressed as:

$$H = \frac{s_2 s_3 \sqrt{\cot^2\phi + 4}}{2\sqrt{3}} \frac{\partial s_1}{\partial \gamma} \tag{11}$$

When the new plastic deformation occurs linearly in a time increment, the new stress relation can be rewrote at the time increment as:

$$\mathbf{s}^*_{new} - 2\mu \triangle \boldsymbol{\varepsilon}^p = \boldsymbol{\alpha} + \sqrt{\frac{2}{3}}\sigma_s \mathbf{n} + \frac{2}{3} H \triangle \boldsymbol{\varepsilon}^p \tag{12}$$

Considering the plastic increment under von Mises yielding condition, the plasticity scalar multiplier can be solved as:

$$\triangle \lambda = \frac{1}{3\mu + H} \sqrt{\frac{3}{2}} \left(\bar{\xi}^*_{new} - \sigma_s \right) \tag{13}$$

where $\bar{\xi}^*_{new} = \sqrt{\frac{3}{2}} \left(\mathbf{s}^*_{new} - \boldsymbol{\alpha} \right) : \mathbf{n}$ is effective trail normal stress. Thus, the cumulative plasticity resistance, deviator stress tensor, effective plastic strain, and effective plastic strain rate can be updated as:

$$\begin{cases} \boldsymbol{\alpha}_{new} = \boldsymbol{\alpha} + \frac{2\sqrt{2}[\bar{\tau}^*_{new} - \tau_s]}{3\mu(3 + H/\mu)} \mathbf{n} \\ \mathbf{s}_{new} = \mathbf{s}^*_{new} - \frac{2\sqrt{2}[\bar{\tau}^*_{new} - \tau_s]}{3 + H/\mu} \mathbf{n} \\ \bar{\varepsilon}_{new} = \bar{\varepsilon} + \frac{2[\bar{\tau}^*_{new} - \tau_s]}{\sqrt{3}\mu(3 + H/\mu)} \\ \dot{\bar{\varepsilon}}_{new} = \frac{2\sqrt{2}[\bar{\tau}^*_{new} - \tau_s]}{3\mu(3 + H/\mu)\triangle t} \end{cases} \tag{14}$$

where $\bar{\tau}^*_{new} = \bar{\xi}^*_{new}/\sqrt{3}$ is effective trail shear stress. $\tau_s = \sigma_s/\sqrt{3}$ is shear flow stress.

4.2 Fracture criterion

In order to obtain the condition that the ASB cracks in the serrated chip, the effective shear stress, effective shear strain, and effective shear strain rate are computed and used in following derivation. Considering the momentum and energy conservation laws and the post-peak constitutive equation of ASB, the continuum governing equations in Lagrangian coordinate system are given as:

Momentum equation: $\rho \dot{v}_s = \gamma_{,y}$ (15)

Energy equation: $\rho c \dot{\theta} = \bar{\tau} \dot{v}_{s,y} - k\theta_{,yy}$ (16)

Constitutive equation: $\bar{\tau} = \bar{\tau}\left(\bar{\tau}_p, \theta, D\right)$ (17)

where $v_s = v \cos\phi / \cos\left(\phi - \gamma_0\right)$ is shear velocity, v is cutting velocity, and γ_0 is rake angle.

The velocity distribution in ASB is assumed to follow the gradient plastic law:

$$v_s = \dot{\bar{\gamma}}_0 \left[y - \frac{\xi}{\pi} \cos\left(\frac{y}{\xi} + \frac{1}{2} \right) \pi + \xi \right], y \in [-\xi, \xi] \tag{18}$$

where $\dot{\bar{\gamma}}_0 = v_s/2\xi$ is mean strain rate in ASB.

The kinematic equation in post-peak stage of constitutive evolution can be estimated through the momentum theorem as:

$$\dot{P}(\xi) = 4\rho\dot{\gamma}\xi\dot{\xi} = \bar{\tau}_p - \bar{\tau} \tag{19}$$

Combining with Eqs. (18) and (19), considering the compatible movement condition: $\dot{U} = 2\dot{\bar{\gamma}}_0 \xi$ and the boundary condition:$\Delta\dot{U}_0 = \Delta U_0 = 0$, the ASB boundary location and the stress collapsing time are solved as:

$$\begin{cases} \xi_c = \frac{3\bar{\tau}_p^2 \Delta t^2}{4\rho \Delta W_c} \\ \Delta t_c = \frac{1}{\bar{\tau}_p} \left(\frac{18\rho \Delta W_c^2}{\dot{\gamma}_c} \right)^{1/3} \end{cases} \tag{20}$$

The critical heat energy rise can be estimated in the small time increment form and the energy equation is approximated as:

$$\underbrace{\rho c \Delta\theta_c}_{\text{heat energy}} \approx \underbrace{\bar{\tau}_p \dot{v}_{s,y} \Delta t_c}_{\text{strain energy}} - \underbrace{k\theta_{,yy} \Delta t_c}_{\text{conducted heat}} \tag{21}$$

The strain energy component and the heat conduction component are estimated as:

$$\begin{cases} \bar{\tau}_p \dot{v}_{S,y} \Delta t_c \approx \frac{\tau_p \Delta U_c}{2\xi} = \frac{\Delta W_c}{2\xi} \\ k\theta_{,yy} \Delta t_c \approx \frac{k \Delta\theta_c \Delta t_c}{4a\xi^2} \end{cases} \tag{22}$$

Accordingly, combining with Eqs. (21) and (22) and adopting the minimum energy dissipation principle, the minimum energy dissipation from the ASB formation to fracture is deduced as:

$$\Delta W_c = 4\rho c \Delta\theta_c \xi \tag{23}$$

The corresponding shear band boundary location and collapsing time are given as:

$$\begin{cases} \xi_c = \left(\frac{9\rho^3 \chi^3 c^2 \Delta\theta_c^2}{2a^3 \bar{\tau}_p^3 \dot{\gamma}_c} \right)^{1/4} \\ \Delta t_c = \frac{6\rho c \Delta\theta_c}{\bar{\tau}_p} \sqrt{\frac{\rho\chi}{2a\bar{\tau}_p \dot{\gamma}_c}} \end{cases} \tag{24}$$

where χ is thermal diffuse coefficient and a is rate-related gradient factor obtained through the shear bandwidth model [26].

The evolution and propagation of ASB are related closely with the energy dissipation, which determined the occurrence condition of ASB fracture. Considering the energy

convergence in ASB in the whole fracture process, the fracture energy G^f_{ASB} can be calculated by the sum of pre-peak energy G_0 and post-peak energy G_P as:

$$\begin{cases} G^f_{ASB} = \int_0^{\bar{\gamma}_c} \bar{\tau} d\gamma = G_0 + G_P \\ G_0 = \int_0^{\bar{\gamma}_o} \bar{\tau}(\bar{\gamma}, \dot{\gamma}, \theta^*) d\gamma \\ G_P = \int_{t_o}^{t_c} \bar{\tau}\left(\bar{\tau}_p, \theta, D\right) \dot{\gamma} dt \approx 6\rho c \Delta\theta_c \sqrt{\frac{\rho\chi\dot{\gamma}_c}{2a\bar{\tau}_p}} \end{cases} \tag{25}$$

Thus, the ASB fracture criterion are given as:

$$G_{ASB} = \int_0^{t_c} \bar{\tau}\dot{\gamma} dt \geq G^f_{ASB} or \frac{\int_{t_o}^{t_c} \bar{\tau}\dot{\gamma} dt}{6\rho c \Delta\theta_c} \sqrt{\frac{2a\bar{\tau}_p}{\rho\chi\dot{\gamma}_c}} \geq 1 \tag{26}$$

5 Finite element analysis

A finite element (FE) model on high-speed machining of α-pure titanium alloy was further developed to analyze the isolated segment chip formation in a 2D plane-strain and thermal–mechanical coupling conditions through ABAQUS/Explicit analytical environment. The FE analysis model is composed by the tool and work material in Lagrange explicit analysis environment as shown in Fig. 9. The workpiece was 3 × 0.5 mm, and the cutting edge radius was 80 μm, the rake angle is − 10°, and the clearance angle is 6°. Considering the mesh controlling condition, the seed size of workpiece was 0.02 mm. The cutting tool was defined as a discrete rigid body with the seed size of 0.1 mm. The element type of workpiece was planar quadrilateral (CPE4RT) with "advancing front" structured meshing technique, and the tool was triangle (CPE3T). Minimizing the mesh transition was selected through the algorithm option to reduce the mesh distortion.

The physical and mechanical parameters of the work material are listed in Table 1, and the constitutive parameters are specified in Table 2 [24]. These parameters were input as the variables defined through the user subroutine. The constitutive framework was adopted in the work material, and the stress–strain relation of the work material was recompiled through VUMAT Fortran subroutine. Considering the kinematic hardening law under the plane strain case, the basic governing equations and the fracture criterion were described in Sects. 3.1 and 3.2.

As for the friction effect due to the interaction between the tool and chip, combining these material constitutive laws, the modified Zorev's friction model was considered by Duan and Zhang [27]; the Coulomb friction and heat transfer models were applied by Wan et al. [28] to simulate the serrated chip formation. Thus, in sliding region, the friction followed the Coulomb friction model (friction coefficient is 0.3 ~ 1.0), and in sticking region, the friction was approximated to be the

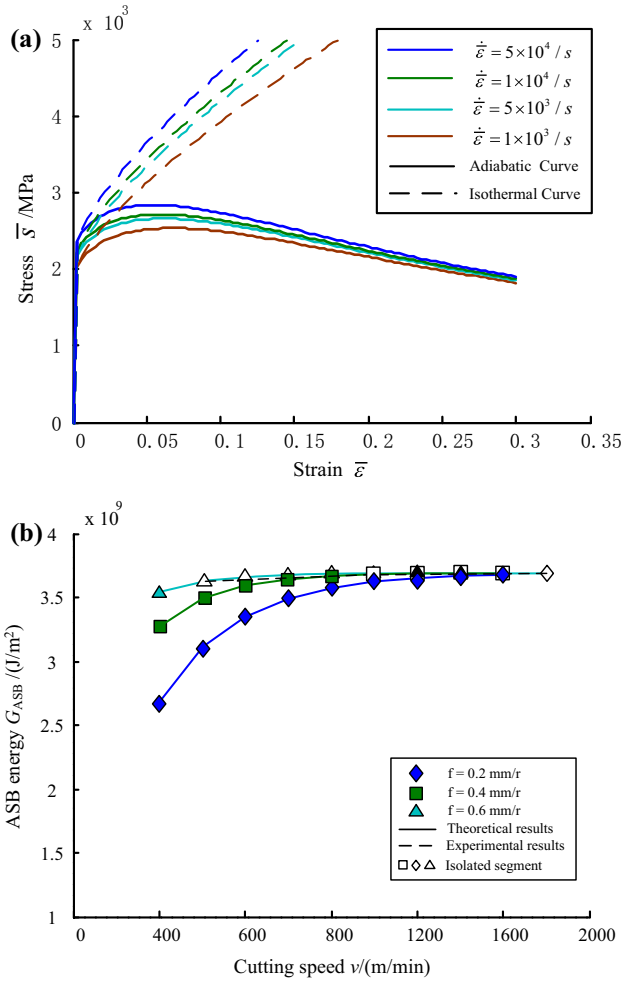

Fig. 9 Constitutive characteristics of α-pure titanium alloy under different loading conditions: (**a**) stress–strain lines under adiabatic and isothermal conditions at different strain rates; (**b**) theoretical and experimental results of energy convergence in ASB

shear stress after the friction stress exceeding the yield shear stress, but was limited by the material strength. Thereby, the finite sliding with penalty contact method was used in the tool-chip interaction. The heat generation mainly results from the plastic deformation and the tool-chip friction. The fraction converting deformation work to heat is about 0.9. The heat transfer coefficient was set according to the experimental result from Filice et al. [29]. In the machining process, large shear deformation and fast shear strain rate occurred in the work material around the tool edge, inducing severe shear damage. A failure zone was adopted to generate the chip, which followed the same constitutive relationship. The separation of the chip from the workpiece was described exactly through shear damage criterion proposed by Calamaz et al. [8]. The chip fracture due to ASLF was controlled by the saturation limit. The simulated chip morphologies were validated and modified through chip geometry and cutting force results.

The stress–strain curve of workpiece element under adiabatic and isothermal conditions is numerically calculated through the described finite element analysis environment and the theoretical and experimental results of energy convergence with cutting speed curve were obtained, as shown in Figs. 9. The stress–strain lines under the strain rates from 1×10^3/s to 5×10^4/s and heat dissipation condition are shown in Fig. 9a. It is shown that the effects of strain hardening and strain rate strengthening are obvious during plastic deformation process. Under the adiabatic conditions, the true stress–strain lines are influenced by the thermal softening effect so that the stress collapses after attaining the peak value. The peak stress means the occurrence of constitutive instability and adiabatic shearing takes place in a relatively small critical strain, resulting in serrated chip formation. Wang et al. [30] suggested that the phase transformation took place in ASB in high-speed machining of Ti6Al4V. This part of energy dissipated due to phase transformation has been considered in degenerating effect in the post-peak constitutive equation. Theoretical and experimental results of energy convergence in ASB are shown in Fig. 9b. The energy limit value of α-pure titanium alloy was found about 3.75×10^9 J/m^2 and is less than the previous experimental results of the hardened carbon steel [31]. Comparing with these materials, Rittel et al. [32] found that the cold work of AM50 steel in the fracture was about 4×10^7 J/m^2. Although the critical strain of ASB fracture considers the strain rate, temperature, and stress state conditions, the physical-related critical condition of ASLF in high-speed machining process still cannot be well revealed. In actual cutting condition, the increase of cutting speed suppressed the heat diffusion and aggravated more energy convergence in ASB. With the cut proceeding, the energy in band gradually accumulated to the saturation limit as the calculated results under wider speed range, resulting in complete separation of serrated segments along shear band.

Being different from the formation mechanisms of serrated chip at relatively low cutting speed, the ASLF process during isolated segment formation at relatively higher cutting speed is complex due to the fast evolution of adiabatic shearing from instability to fracture. The simulated results of isolated segment chip formation in the form of equivalent plastic strain contours at cutting speed of 1600 m/min are shown in Fig. 10. Some of the overlapped elements were removed in the simulated results for clear display. The ASLF process of isolated segment formation is divided into three stages through the quick-stop experimental results. In the onset stage of adiabatic shearing as shown in Fig. 10a, the shear band region is conceived from the tool tip and propagates to free surface. Subsequently, the internal cracking in the shear band region from the tool tip to the free surface is shown in Fig. 10b–d. The compression zone in the physical model as shown in Fig. 9a is verified according to the deformation and stress contours. Meanwhile, the high heating convergence in the shear band region leaded to thermal softening effect, and thus the internal cracking was suppressed, which leads to cold welding between the fractured shear band surfaces near the chip bottom, resulting in adhesive between the neighboring two segments. The ASLF is a sudden fracture phenomenon, and the free surface cracking is only observed according to the experiment of Gu and Wang [31]. The final stage of isolated segment chip formation as shown in Fig. 10e illustrates the complete fracture along ASB. These simulated results are verified through the obtained chip root sample in Fig. 10f. The formation process of isolated segment chip has been studied in experimental and simulative methods. There were two mechanisms that free surface crack and internal crack explaining the fracture of isolated segment. The internal cracking before the segment formation was observed by Guo and Yen [10]. The free surface crack was also observed in machining hardened steel by Poulachon and Moisan [22] due to hardening effect on the machined surface. In our analysis results, the internal crack propagated from the tool tip to the free surface due to the concentrated heat and deformation, resulting in brittle-ductile transient of ASLF process. This brittle effect in serrated segment fracture was also found in the high-speed hard cutting by Wang and Liu [14]. It indicated that high strain rate induced the strengthening effect in chip material enhanced the mechanical performance that leaded to abrupt brittle-ductile fracture under high cutting speed condition.

The simulated results of the corresponding equivalent stress contours during isolated segment chip formation are shown in Fig. 11 where the units and dimensions are in accordance with Fig. 9a. The stress distributed inhomogenously on the two sides of ASB. In Fig. 11a, the stress region is wider in the matrix in front of ASB due to the extrusion effect of cutting tool. The maximum stress near the shear plane is about 2.2×10^3 MPa which approximates the peak stress under adiabatic condition shown in Fig. 9a. The stress concentration on free surface also approximates the peak stress. With the deformation localization proceeding in shear band after the

Fig. 10 Simulated results of equivalent plastic strain contour describing the formation process of isolated segment chip of α-pure titanium alloy and the experimental result of chip root sample ▶

Table 2 The constitutive parameters of α-pure titanium alloy

A (MPa)	B (MPa)	n	C	m_1	m_2	$\dot{\varepsilon}_0$	θ_M(K)	θ_0(K)
150	797	0.75	0.1	6.375	–0.005	0.001	1965	300

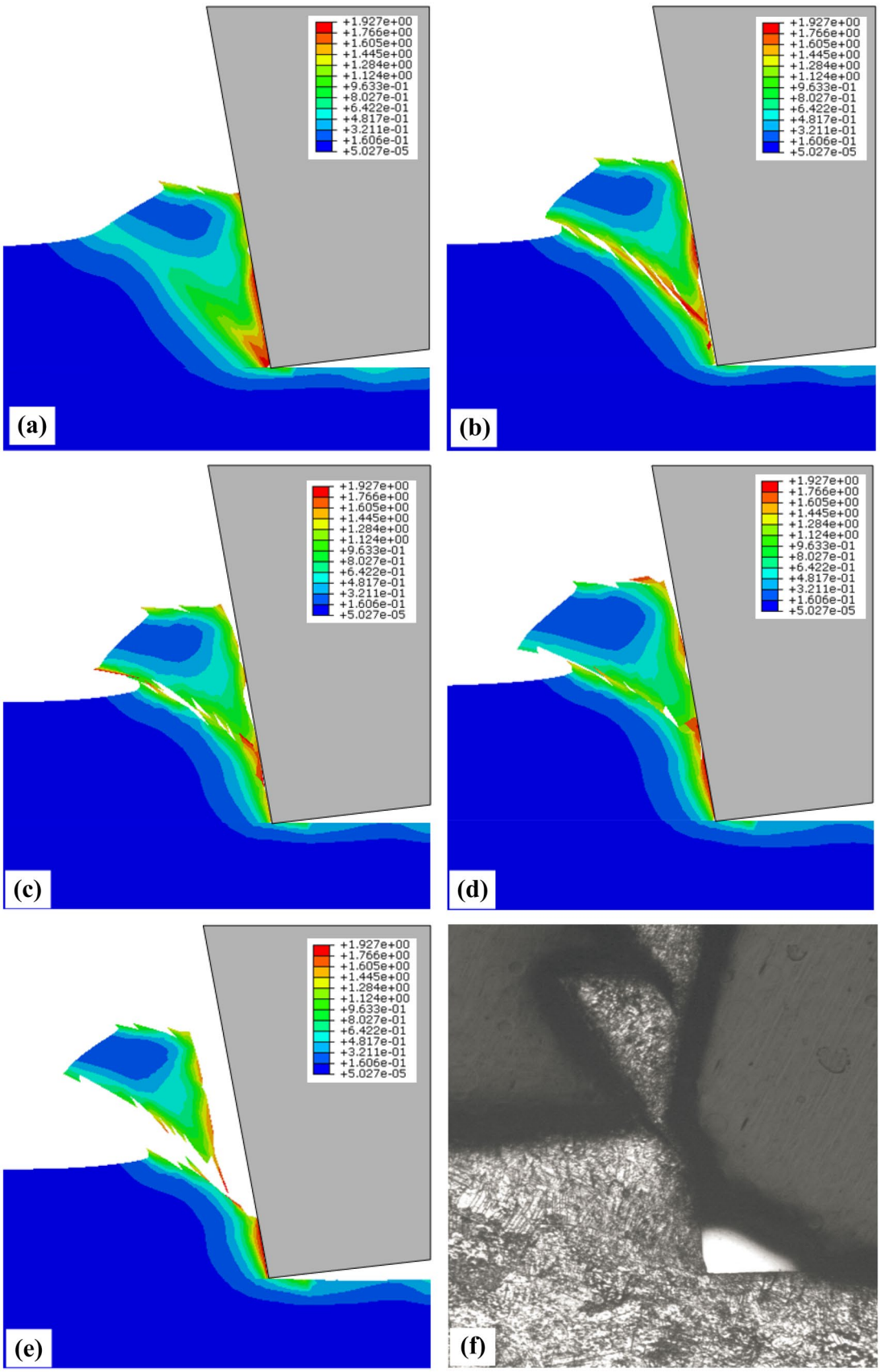
+1.927e+00
+1.766e+00
+1.605e+00
+1.445e+00
+1.284e+00
+1.124e+00
+9.633e-01
+8.027e-01
+6.422e-01
+4.817e-01
+3.211e-01
+1.606e-01
+5.027e-05
(a)
(b)
(c)
(d)
(e)
(f)

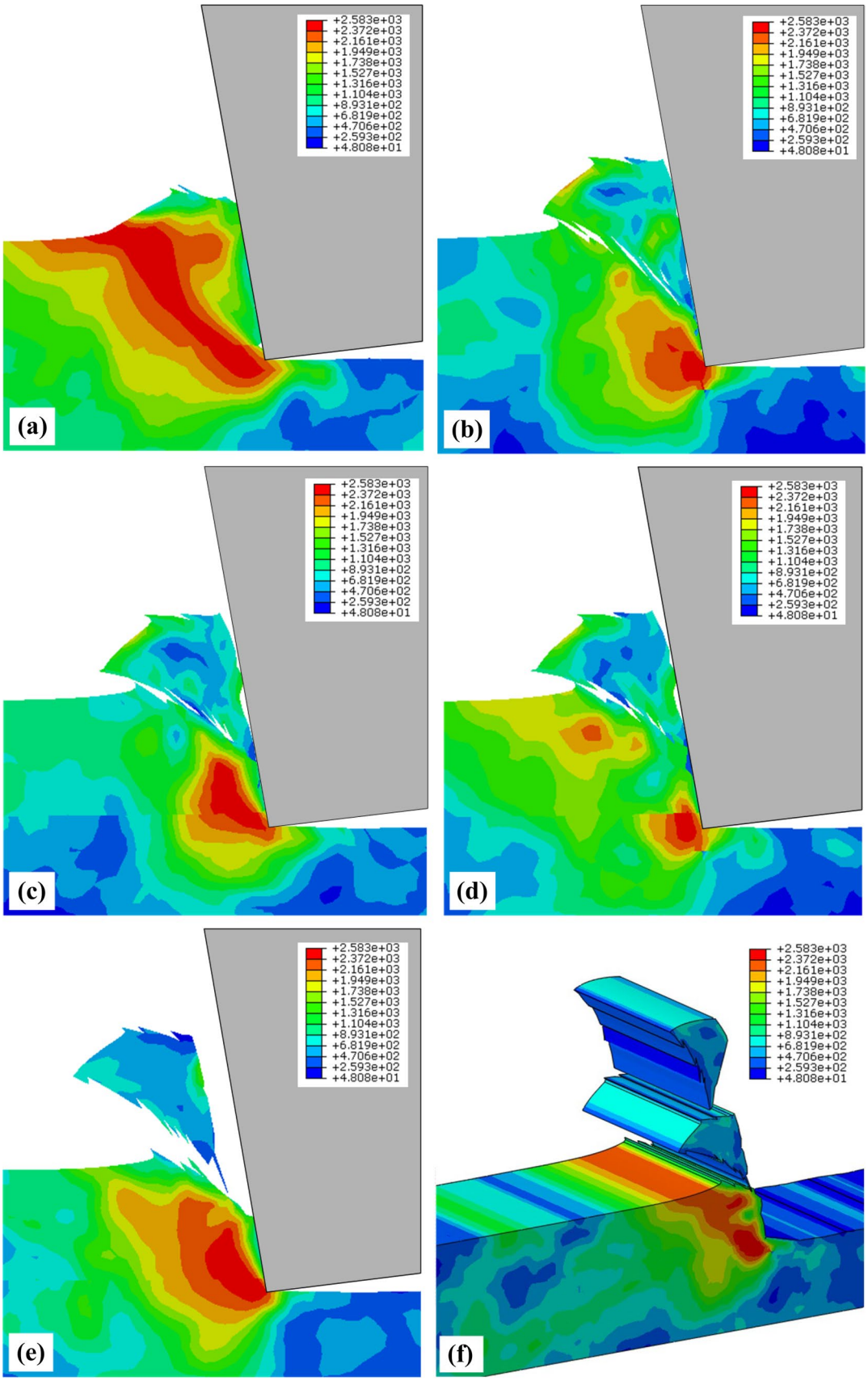

Fig. 11 Simulated results of equivalent stress contours describing the formation process of isolated segment chip of α-pure titanium alloy and the 3D stereogram

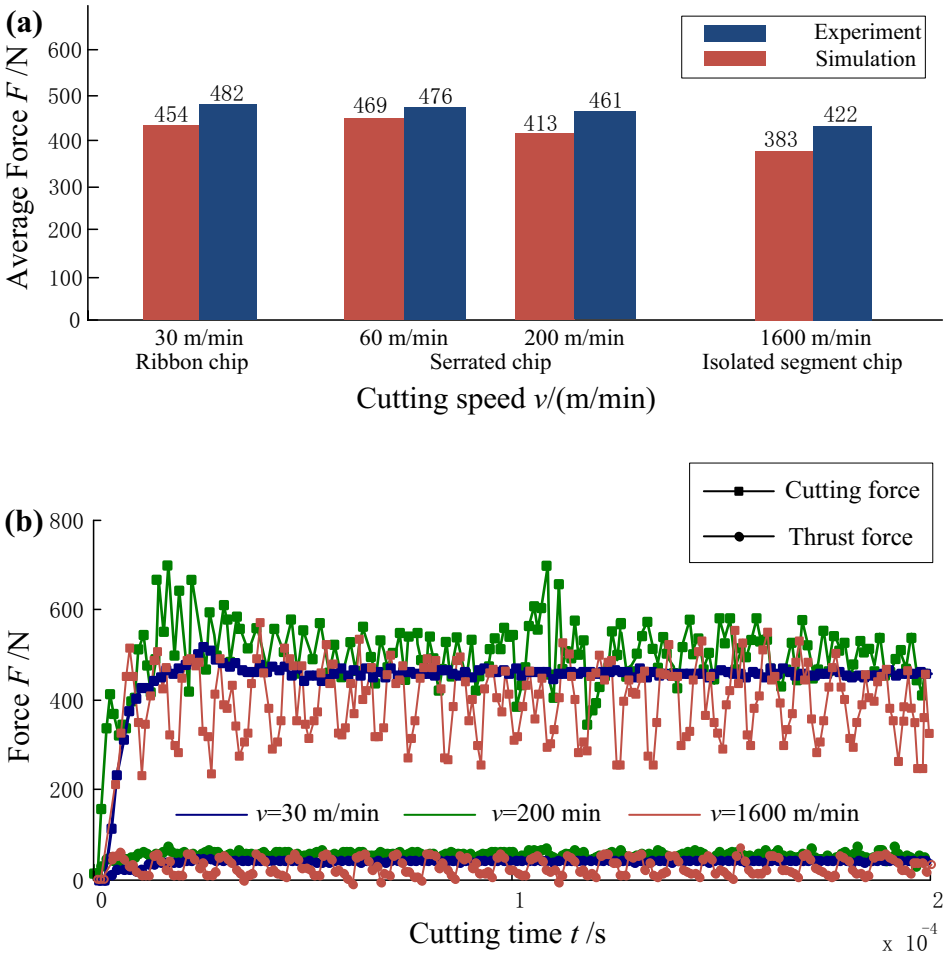

Fig. 12 The simulated and experimental results of the average forces with (**a**) the various chip types of α-pure titanium alloy and (**b**) the corresponding force fluctuations in the cutting direction and thrust direction at various cutting speeds

stress exceeding the peak value, the stress began to collapse due to the thermo-weakening effect from damage to cracking in the middle of ASB (Fig. 11b, c). The stress near the crack was decreased from the peak stress to 9×10^2 MPa approximately. The stress on free surface was released when the crack propagates completely along ASB. The cold welding effect between the isolated segment and the workpiece could lead to the residue stress about 6×10^2 MPa on the fractured band surface (Fig. 11d). The stress rapidly decreased to a lowest level when the isolated segment formed (Fig. 11e). The fracture of the isolated segment made the cutting process discontinuous, resulting in the fluctuation of residual stress on the machined surface along the cutting direction, as shown in Fig. 11f. It can be deduced that the temperature in segment mainly concentrated in the middle of ASB and the chip bottom which induces white layer formation under the friction effect. The deformation mainly concentrated in ASB and chip bottom, which leaded to higher temperature and grain fragmentation in these two regions. Therefore, the competition between work hardening effect and thermal softening effect, as well as the degenerating effect due to the damage in ASB, closely influenced the effective stress distribution which determined the fracture mechanism and the occurrence condition of ASLF.

Through detecting the cutting force along the cutting direction and the thrust force perpendicular to the cutting direction via the YBF strain gauge dynamometer, the simulated and experimental results of the average forces with the various chip types and the corresponding force fluctuations at various cutting speeds are shown in Fig. 12. The ribbon chip was formed in a single deformation process with stable average values that the cutting force was 454 N and the thrust force was 50 N at relatively low speed of 30 m/min. Under the cutting speed from 60 to 200 m/min, the chip deformation process turned to be unstable due to adiabatic shearing. The cutting force and the thrust force appeared obvious fluctuation due to the periodic localized deformation in primary shear zone during the serrated segment formation. Due to the chip deformation in primary shear zone experiencing the peak stress, the cutting force was increased to 469 N at first and then decreased to 413 N due to the serrated effect and thermal effect. The fluctuation in the cutting process was increasingly obvious due to the cracking in shear band when the cutting speed was above 200 m/min. With the crack propagation in shear band under the increasing cutting speed, an obvious increase of fluctuation amplitude in the cutting force and thrust force was obtained when the cutting speed was up

to 1600 m/min (Fig. 12b). The average force decreased with the cutting speed, while the simulated forces were relatively smaller due to ignoring the tool wear on the cut edge. Similar average force patterns were also observed by Guo and Yen [10] in cutting AISI 4340 steel and by Kumbera et al. [33] in cutting silicon nitride. The average cutting force decreased comparing with the ribbon chip and the serrated chip without cracking, which was also found by Wang and Liu [34]. The analytical results indicated that the developed constitutive modeling with the fracture criterion well coincided with the experimental results.

6 Conclusions

1. The chip morphology was observed microscopically through high-speed machining of α-pure titanium alloy and its quick-stop tests. The negative rake angle and large feed shortened the cutting speed range of adiabatic shear evolution, prompting the isolated segment chip formation. The austenite grains in shear band material were tore to small pieces, and the austenite twins were observed in the chip segment due to cutting deformation. The smooth surface formed, and the melting trace was not observed on the fractured surface due to the cold welding and cracking between the segments.
2. The pre-peak and post-peak constitutive model with kinematic hardening law and an energy failure criterion of ASLF were further developed into the finite element subroutine. The stress–strain relationship and the energy-cutting speed relationship were numerically calculated. The increase of ASB energy was sensitive to the cutting speed and feed under negative rake angle. The limit energy value in ASB of α-pure titanium alloy was relatively small comparing with the hardened steels.
3. The ASLF in high-speed cutting of α-pure titanium alloy was closely related to its energy convergence. The internal crack nucleation and propagation along ASB were simulated in the formation of isolated segment chip of α-pure titanium alloy. The competition between work hardening effect and thermal softening effect, as well as the degenerating effect, determines the fracture mechanism and the occurrence condition of ASLF.
4. High cutting speed induced strengthening effect leads to abrupt brittle-ductile fracture in ASB during isolated segment formation. Higher fluctuation amplitude of cutting force and lower average cutting force were found in isolated segment chip formation comparing with the serrated chip at relatively lower cutting speed.

Appendix v : Cutting velocity ($m{\cdot}s^{-1}$); v_s: Shear velocity ($m{\cdot}s^{-1}$); v_{ch}: Chip flow velocity ($m{\cdot}s^{-1}$); x, y: Coordinate axis (m); t: Time (s); a: Rate-related gradient factor; a_c: Uncut thickness (m); a_{ch}: Chip thickness (m); ϕ : Shear angle (°); σ_b: Tensile strength (MPa); σ_s: Yield strength (MPa); δ: Elongation (%); φ: Reduction of area (%); U: Upper side displacement of shear band region (m); S: Shear bandwidth (μm); ζ : Deformation coefficient of serrated segment; ξ : Boundary location of shear band region (m); ξ^*_{new} : Effective trail normal stress (MPa); $\boldsymbol{\sigma}$: Stress tensor (MPa); $\boldsymbol{\varepsilon}$: Strain tensor; $\dot{\varepsilon}$: Strain rate tensor (s^{-1}); $\mathbf{D}$: Hooke tensor; Δ: Time increment interval; $\Delta\lambda$: Plasticity scalar multiplier; λ, μ: Lamés constants; $f_s \geq 0$: Yield condition; $\mathbf{n}$: Unit yield vector; $\mathbf{s}$: Deviator stress tensor (MPa); $\mathbf{s}^*_{new}$: Trail elastic stress (MPa); $\boldsymbol{\alpha}$: Cumulative plasticity resistance (MPa); $\Delta\boldsymbol{\alpha}$: Plasticity hardening law (MPa); $\tilde{\sigma}$: Effective normal stress (MPa); $\overline{\varepsilon}$: Effective normal strain; $\dot{\overline{\varepsilon}}$: Effective normal strain rate (s^{-1}); $[\sigma_i]$: Principal stress components (MPa); $[\varepsilon_i]$: Principal strain components; $[\dot{\varepsilon}_i]$: Principal strain rate components (s−1); δ_{ij}: Kronecker delta function; σ: Normal stress (MPa); τ: Shear stress (MPa); $\overline{\tau}$: Effective shear stress (MPa); $\overline{\gamma}$: Effective shear strain; $\dot{\overline{\gamma}}$: Effective shear strain rate (s^{-1}); $\overline{\tau}_p$: Equivalent peak stress (MPa); $\overline{\tau}(\gamma, \dot{\gamma}, \theta)$: Pre-peak constitutive relation (MPa); $\overline{\tau}(\overline{\tau}_p, \theta, D)$: Post-peak constitutive relation (MPa); s_1, s_2, s_3: Constitutive components; A, B, C, m, n: Constitutive parameters; γ: Shear strain; $\dot{\gamma}$: Shear strain rate (s^{-1}); $\dot{\overline{\gamma}}_0$: Mean strain rate ($s^{-1}$); γ_0: Rake angle (°); l_s: Undeformed thickness of serrated segment; L_s: Shear band space (m); θ: Temperature (K); θ^*: Characteristic temperature; θ_0: Initiate temperature (K); θ_m: Melt point (K); ρ: Mass density ($kg{\cdot}m^{-3}$); c: Thermal specific capacity ($J{\cdot}kg^{-1}{\cdot}K^{-1}$); $C_{\tilde{\xi}}$: Boundary propagation speed of ASB; D: Degenerating coefficient; $\tilde{H}$: Hardening effect; χ: Thermal diffuse coefficient ($m^2{\cdot}s^{-1}$); α: Thermal weakening factor; β: Taylor and Quinney coefficient; W_c: Critical energy dissipation ($J{\cdot}m^{-2}$); G^f_{ASB} : Fracture energy($J{\cdot}m^{-2}$; G_0: Pre-peak energy ($J{\cdot}m^{-2}$); G_P: Post-peak energy ($J{\cdot}m^{-2}$)

Funding This study was funded by the National Natural Science Foundation of China [Award Number: 51175063] and the Fundamental Research Funds for the Central Universities [Award Number: 2682020CX33]. Thanks for the support from the Dalian University of Technology and Southwest Jiaotong University.

Declarations

Ethics approval Not applicable.

Consent to participate Not applicable.

Consent for publication Not applicable.

Conflict of interest/competing interests The authors declare no competing interests.

References

1. Sima M, Özel T (2010) Modified material constitutive models for serrated chip formation simulations and experimental validation in machining of titanium alloy Ti–6Al–4V. Int J Mach Tools Manuf 50:943–960
2. Zhang X, Wu S, Wang H, Liu CR (2011) Predicting the effects of cutting parameters and tool geometry on hard turning process using finite element method. J Manuf Sci Eng 133:041010
3. Wu H, To S (2015) Serrated chip formation and their adiabatic analysis by using the constitutive model of titanium alloy in high speed cutting. J Alloy Compd 629:368–373

4. Hokka M, Gomon D, Shrot A, Leemet T, Bäker M, Kuokkala V-T (2013) Dynamic behavior and high speed machining of Ti-6246 and alloy 625 superalloys: experimental and modeling approaches. Exp Mech 54:199–210
5. He L, Su H, Xu J, Zhang L (2018) Simulation analysis of the influence of dynamic flow stress behavior on chip formation. Int J Adv Manuf Technol 95:2301–2313
6. Gao C-Y, Zhang L-C, Liu P-H (2016) The role of material model in the finite element simulation of high-speed machining of Ti6Al4V. Proc Inst Mech Eng C J Mech Eng Sci 230:2959–2967
7. Shuang F, Chen X, Ma W (2018) Numerical analysis of chip formation mechanisms in orthogonal cutting of Ti6Al4V alloy based on a CEL model. IntJ Mater Form 11:185–198
8. Calamaz M, Coupard D, Girot F (2008) A new material model for 2D numerical simulation of serrated chip formation when machining titanium alloy Ti–6Al–4V. Int J Mach Tools Manuf 48:275–288
9. Che J, Zhou T, Liang Z, Wu J, Wang X (2018) Serrated chip formation mechanism analysis using a modified model based on the material defect theory in machining Ti-6Al-4 V alloy. Int J Adv Manuf Technol 96:3575–3584
10. Guo Y, Yen D (2004) A FEM study on mechanisms of discontinuous chip formation in hard machining. J Mater Process Technol 155:1350–1356
11. Hua J, Shivpuri R (2004) Prediction of chip morphology and segmentation during the machining of titanium alloys. J Mater Process Tech 150:124–133
12. Ye GG, Xue SF, Jiang MQ, Tong XH, Dai LH (2013) Modeling periodic adiabatic shear band evolution during high speed machining Ti-6Al-4V alloy. Int J Plast 40:39–55
13. Ma W, Chen X, Shuang F (2017) The chip-flow behaviors and formation mechanisms in the orthogonal cutting process of Ti6Al4V alloy. J Mech Phys Solids 98:245–270
14. Wang B, Liu Z (2014) Investigations on the chip formation mechanism and shear localization sensitivity of high-speed machining Ti6Al4V. Int J Adv Manuf Technol 75:1065–1076
15. Cui X, Zhao B, Jiao F, Zheng J (2016) Chip formation and its effects on cutting force, tool temperature, tool stress, and cutting edge wear in high-and ultra-high-speed milling. Int J Adv Manuf Technol 83:55–65
16. Gu L, Wang M, Chen H, Kang G (2016) Experimental study on the process of adiabatic shear fracture in isolated segment formation in high-speed machining of hardened steel. Int J Adv Manuf Technol 86:671–679
17. Gu L, Kang G, Chen H, Wang M (2016) On adiabatic shear fracture in high-speed machining of martensitic precipitation-hardening stainless steel. J Mater Process Technol 234:208–216
18. Gente A, Hoffmeister H, Evans C (2001) Chip formation in machining Ti6Al4V at extremely high cutting speeds. CIRP Ann Manuf Technol 50:49–52
19. Barry J, Byrne G, Lennon D (2001) Observations on chip formation and acoustic emission in machining Ti6Al4V alloy. Int J Mach Tools Manuf 41:1055–1070
20. Lee W-S, Chiu C-C (2006) Deformation and fracture behavior of 316L sintered stainless steel under various strain rate and relative sintered density conditions. Metall Mater Trans A 37A:3685–3696
21. Elbestawi M, Srivastava A, El-Wardany T (1996) A model for chip formation during machining of hardened steel. CIRP Ann Manuf Technol 45:71–76
22. Poulachon G, Moisan A (2000) Hard turning: chip formation mechanisms and metallurgical aspects. J Manuf Sci Eng 122:406
23. Gu L-Y, Wang M-J (2018) Adiabatic shear fracture prediction in high-speed cutting at various negative rake angles and feeds. Adv Manuf 6:41–51
24. Gu L (2018) Critical condition prediction of adiabatic shear fracture in high-speed cutting TA2 alloy. Int J Adv Manuf Technol 94:2981–2991
25. Liao SC, Duffy J (1998) Adiabatic shear bands in a Ti-6Al-4V titanium alloy. J Mech Phys Solids 46:2201–2231
26. Dodd B, Bai Y (1989) Width of adiabatic shear bands formed under combined stresses. Mater Sci Technol 5:557–559
27. Duan C, Zhang L (2012) A reliable method for predicting serrated chip formation in high-speed cutting: analysis and experimental verification. Int J Adv Manuf Technol 64:1587–1597
28. Wan L, Wang D, Gao Y (2016) The investigation of mechanism of serrated chip formation under different cutting speeds. Int J Adv Manuf Technol 82:951–959
29. Filice L, Umbrello D, Micari F, Settineri L (2007) On the finite element simulation of thermal phenomena in machining processes. Ed: Springer Berlin Heidelberg 263–278
30. Wang Q, Liu Z, Yang D, Auh M (2017) Metallurgical-based prediction of stress-temperature induced rapid heating and cooling phase transformations for high speed machining Ti-6Al-4V alloy. Mater Des 119:208–218
31. Gu L, Wang M, Duan C (2013) On adiabatic shear localized fracture during serrated chip evolution in high speed machining of hardened AISI 1045 steel. Int J Mech Sci 75:288–298
32. Rittel D, Wang Z, Merzer M (2006) Adiabatic shear failure and dynamic stored energy of cold work. Phys Rev Lett 96:75502
33. Kumbera T, Patten J, Cherukuri H, Brand C, Marusich T (2001) Machining force analysis for ductile machining of silicon nitride. J Manuf Sci Technol 5:341–352
34. Wang B, Liu Z (2015) Shear localization sensitivity analysis for Johnson-Cook constitutive parameters on serrated chips in high speed machining of Ti6Al4V. Simul Model Pract Theory 55:63–76